



OPEN

Precipitation trends determine future occurrences of compound hot-dry events

Emanuele Bevacqua¹✉, Giuseppe Zappa², Flavio Lehner^{3,4} and Jakob Zscheischler^{1,5,6}

Compound hot-dry events—co-occurring hot and dry extremes—frequently cause damages to human and natural systems, often exceeding separate impacts from heatwaves and droughts. Strong increases in the occurrence of these events are projected with warming, but associated uncertainties remain large and poorly understood. Here, using climate model large ensembles, we show that mean precipitation trends exclusively modulate the future occurrence of compound hot-dry events over land. This occurs because local warming will be large enough that future droughts will always coincide with at least moderately hot extremes, even in a 2 °C warmer world. By contrast, precipitation trends are often weak and equivocal in sign, depending on the model, region and internal climate variability. Therefore, constraining regional precipitation trends will also constrain future compound hot-dry events. These results help to assess future frequencies of other compound extremes characterized by strongly different trends in the drivers.

When hot and dry extreme conditions coincide, the resulting impacts on humans and ecosystems are often disproportionate. For example, compound hot-dry events cause tree mortality, crop losses and wildfire, with wide-ranging socioeconomic effects^{1–5}. Sustained compound hot and dry conditions can critically reduce streamflow and cause water shortages, representing a threat for agriculture and food security^{6–8}. Given the suite of impacts, the present and future dynamics of compound hot-dry events have received considerable attention from the scientific community over recent years^{9–12}.

Previous studies have focused on assessing the frequency of compound hot-dry events (f_{HD}), which is crucial for developing strategies to cope with the compound-event impacts. In a warmer climate, higher temperatures will increase f_{HD} by causing more-frequent hot events everywhere over land^{6,9,10,13}. In addition, mean precipitation is expected to change over most land masses in response to global warming^{14,15}, but its importance for future changes in f_{HD} is unknown. Furthermore, available f_{HD} estimates are based either on observations or on routinely used climate model outputs, which—due to limited sample sizes—prevent a systematic understanding of present and future uncertainties in compound-event occurrence. In particular, such limited sample sizes do not allow for distinguishing between irreducible and reducible f_{HD} uncertainties, which arise from internal climate variability (that is, from the inherent chaotic nature of the climate system)¹⁶ and structural differences between climate models, respectively. Understanding the source of these uncertainties may ultimately allow for reducing them and therefore inform the development of costly socioeconomic adaptation strategies to climate change¹⁷. In this article, employing climate model output from an ensemble of seven single-model initial-condition large ensembles¹⁶ (SMILEs), we address these research gaps; that is, we reveal the importance of mean precipitation trends for future f_{HD} , and investigate present and future uncertainties in f_{HD} and their sources. We focus on historical conditions (1950–1980) and a future climate that is—in line with the Paris Agreement—about 2 °C warmer than pre-industrial conditions.

To estimate the influence of internal climate variability, each of the seven SMILEs is run multiple times from different initial conditions, resulting in multiple ensemble members that span a range of plausible climates and associated f_{HD} . The multimodel mean of this f_{HD} range provides an estimate of the uncertainty in f_{HD} in a single realization due to internal climate variability¹⁸ (U_{IV}). Uncertainty due to model-to-model differences in f_{HD} (U_{MD}) are estimated on the basis of the intermodel range of the ensemble mean of f_{HD} (see Methods for details).

We focus on land masses and characterize hot-dry events on the basis of temperature and precipitation means over the warm season (the climatologically hottest three consecutive months), which is when the impacts from the compound event are generally most pronounced⁹. We highlight that our main conclusions also apply to the wettest season, which for some regions may be the season where impacts from the compound event are largest. To study the concurrence of hot and dry conditions, we compute f_{HD} as the empirical frequency (%) of concurrent extremes, that is, the count of simultaneous exceedances of temperature over its historical 90th percentile and precipitation below its historical 10th percentile (individual extremes occurring every ten years on average) divided by the total number of considered seasons^{9,19}.

Uncertainty in historical estimates

The global average of f_{HD} over land during the historical period (1950–1980) is about 3% (Fig. 1a; compound events occurring every 33 years on average), which implies compound hot-dry events are three times more likely to occur than expected under independence between temperature and precipitation (1% probability). These estimates are in line with earlier results based on observations and climate model simulations⁹ and are controlled by the negative correlations between temperature and precipitation over land ($\text{cor} = -0.42$ on average) caused by a combination of atmospheric processes and land-atmosphere interactions²⁰.

Using large-ensemble simulations from multiple models demonstrates that large sample sizes are crucial for robust estimates

¹Department of Computational Hydrosystems, Helmholtz Centre for Environmental Research – UFZ, Leipzig, Germany. ²National Research Council of Italy, Institute of Atmospheric Sciences and Climate (CNR-ISAC), Bologna, Italy. ³Department of Earth and Atmospheric Sciences, Cornell University, Ithaca, NY, USA. ⁴Climate and Global Dynamics Laboratory, National Center for Atmospheric Research, Boulder, CO, USA. ⁵Climate and Environmental Physics, University of Bern, Bern, Switzerland. ⁶Oeschger Centre for Climate Change Research, University of Bern, Bern, Switzerland. ✉e-mail: emanuele.bevacqua@ufz.de

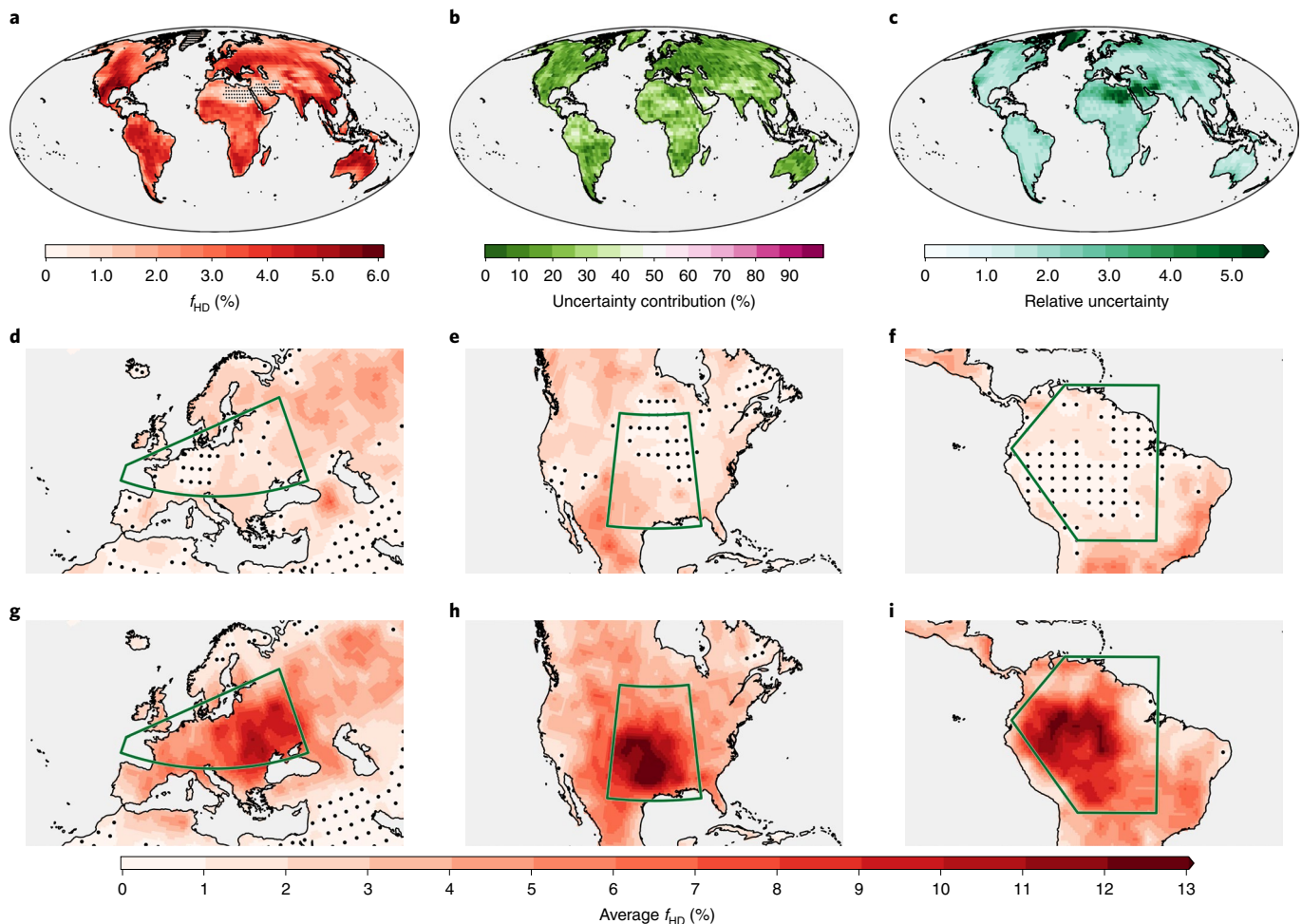


Fig. 1 | Historical f_{HD} and associated uncertainties. **a**, Multimodel mean of f_{HD} during the warm season (1950–1980). **b**, Uncertainty in f_{HD} due to U_{MD} relative to the sum of U_{MD} and U_{IV} (expressed in percentage; uncertainty is dominated by internal climate variability for values below 50% and by model-to-model differences otherwise; Methods). **c**, Uncertainty in f_{HD} due to internal climate variability ($2 \times U_{IV}$) relative to f_{HD} . **d–i**, Average of the f_{HD} spatial fields associated with the lowest (**d–f**) and highest (**g–i**) 7% regionally averaged f_{HD} among a pool of ensemble members from different climate models (Methods), shown for three of the regions used in the IPCC: Central Europe (**d,g**), Central North America (**e,h**) and Amazon (**f,i**). Stippling in panels **a** and **d–i** indicates areas where f_{HD} is smaller than expected under independence between precipitation and temperature.

of f_{HD} . Overall, model differences in f_{HD} are relatively small (Fig. 1b). By contrast, estimates of f_{HD} based on a single climate realization are highly uncertain because of internal climate variability (Fig. 1c), indicating a wide range of possible compound-event risk estimates. For example, the compound-event frequency $f_{HD} \pm U_{IV}$, where the range $\pm U_{IV}$ is an estimate of the 68% uncertainty range (Methods), is $3.6 \pm 3.5\%$ at the grid cell containing Paris, France. At the global scale, the relative uncertainty $2 \times U_{IV}/f_{HD}$ is 2.3 on average. Notably, the same metric for the frequency of (univariate) hot extremes derived from the same 31 years of data is 1.1, whereas to reach a relative uncertainty of 1.1 in f_{HD} requires 130 years of data (Extended Data Fig. 1). This highlights that estimates of compound-event frequencies are substantially more uncertain than related univariate estimates.

The uncertainty in local f_{HD} is reflected in estimates at the regional scale, which are often of interest for defining climate adaptation strategies²¹. For example, for Central Europe, Central North America and Amazon, which are at a relatively high risk of compound hot–dry events^{9,22} (Fig. 1a), the bottom 7% regionally averaged f_{HD} estimates among the ensemble members indicate frequencies in line with independence between temperature and

precipitation (stippling in Fig. 1d–f), which are up to 13 times smaller than in the top 7% members (Fig. 1g–i). We conclude that estimates of the occurrence of compound hot–dry events based on relatively short climate data such as observations (<130 years) can be highly misleading as they may, by chance, indicate low compound-event risk in areas that are, instead, at high risk (or vice versa).

Trends in mean precipitation as key modulator

In a warmer climate, the global average frequency of compound hot–dry events is projected to increase to a land average of about 12% (multimodel range: 10–14%), or about four times higher compared with 1950–1980 (Fig. 2a)⁹. Compared with the historical period, the uncertainty in the f_{HD} estimates can be enhanced by model differences in the response to climate change and particularly in the projected regional mean warming and mean precipitation trends¹⁸. This would be expected as, for both temperature and precipitation, trends in mean conditions drive changes in extremes^{23,24}, and therefore uncertainty in trends can affect future occurrences of univariate and compound extremes. Accordingly with this expectation, the uncertainty in local temperature trends leads to a large

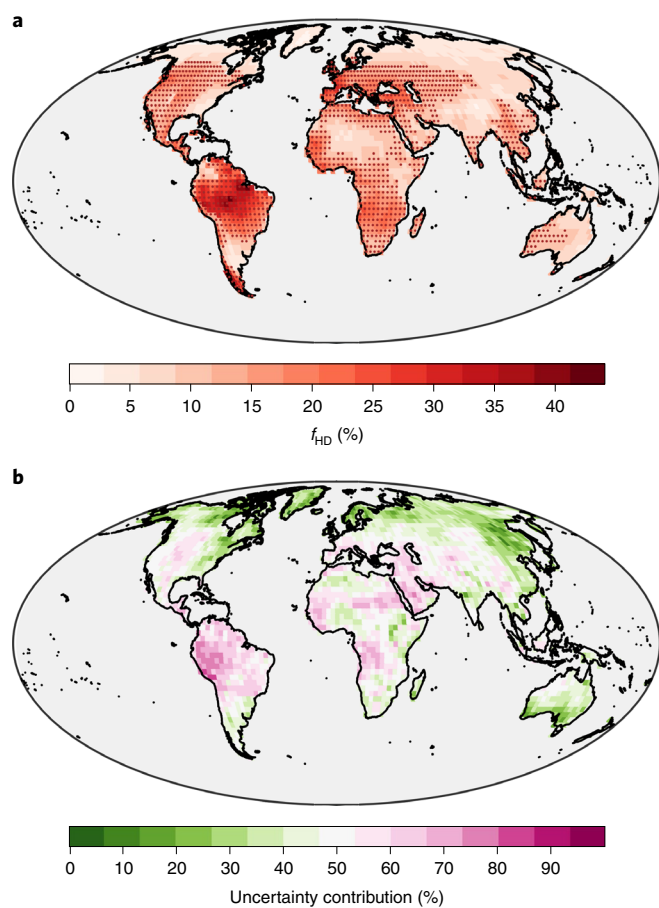


Fig. 2 | f_{HD} in a 2°C world and associated drivers of uncertainties.

a, Multimodel mean of f_{HD} during the warm season in a climate 2°C warmer than pre-industrial conditions. Stippling indicates values above 10%, which is the projected f_{HD} if only temperature increases with no changes in precipitation (see the first discussion item in Supplementary Information). **b**, Uncertainty in f_{HD} due to model-to-model differences (U_{MD}) relative to the sum of U_{IV} and U_{MD} (uncertainty is dominated by internal climate variability for values below 50% and by model-to-model differences otherwise; Methods).

uncertainty range in the future frequency of hot events (f_H) of 38% on average worldwide (Fig. 3a,b; Extended Data Fig. 2c shows that model differences dominate the uncertainty in warming trends). Nevertheless, we find that the uncertainty in local warming trends does not affect future f_{HD} because nearly all dry events will be extremely hot regardless of the exact local warming level⁶ (uncertainty range in future f_{HD} is less than 1.5% on average, Fig. 3a,c). In particular, future temperature is higher than the historical 90th percentile for 96% of droughts on average over land masses according to the multimodel mean. This occurs because trends normalized by the standard deviation in the year-to-year variability are much larger for temperature than for precipitation (Extended Data Fig. 3a,b and Supplementary Information). Even under moderate warming of 2°C, this mechanism is effective over virtually all land masses (Fig. 3c), including regions characterized by a weaker increase in hot extreme occurrences such as Argentina, Australia and India^{25,26} (Extended Data Fig. 2a).

The situation is very different for precipitation trends, which strongly influence uncertainties in future f_{HD} (uncertainty range of 48% on average, Fig. 3d,e). Consequently, projected precipitation trends also strongly determine f_{HD} in a warmer world.

In particular, models projecting a stronger increase in mean precipitation are associated with a lower frequency of concurrent hot and dry events in the future, and vice versa (mean correlation of -0.8 , Fig. 3f). This relationship also holds when considering higher thresholds to define extremes, that is, potentially more impactful compound events, compound hot–dry events during the wettest season (Extended Data Fig. 4a–d) and other warming levels, as long as local warming trends are large compared with local precipitation trends (Extended Data Fig. 5 and Supplementary Information). Furthermore, while the underlying negative correlations between temperature and precipitation may favour the exclusive control of precipitation trends on future f_{HD} , results are similar when assuming zero correlation (Extended Data Figs. 5 and 6 and Supplementary Information). This indicates that a similar mechanism may govern the future dynamics of other compound events that are affected by global warming and for which trends in the drivers differ strongly in magnitude, regardless of the underlying dependencies between the compound-event drivers^{27,28}. For example, the results are similar when considering compound hot–dry events defined on the basis of soil moisture rather than precipitation, that is, on the basis of soil moisture drought rather than meteorological drought (Extended Data Fig. 4e,f). Other events may include, for example, compound high-temperature and low-chlorophyll extremes in the ocean, which threaten marine ecosystems²⁹, sequential flood–heatwave events that slow recovery times and amplify damages³⁰ as well as emerging novel combinations of extreme weather such as tropical cyclone–deadly heat compound events³¹.

Overall, our results imply that improved modelling of precipitation trends is needed^{32,33} to reduce uncertainties in the projection of future f_{HD} . However, we also find that about half of the uncertainty in precipitation trends (Extended Data Fig. 7c), and therefore in the future f_{HD} (Fig. 2b), is driven by internal climate variability over the majority of land masses. This means that even if precipitation trends could be constrained for some regions^{34–36}, uncertainties would remain high for most land areas due to ‘certain uncertainty’ from unpredictable internal climate variability³⁷. Hence, given model and internal variability uncertainties, for practical risk assessment, considering distinct plausible precipitation trends, that is, different climate storylines^{38–41}, may be a way to plan for plausible future compound-event risk.

Estimating future compound-event occurrences

Across all large-scale regions commonly used in the Intergovernmental Panel on Climate Change, the regional average of the future f_{HD} associated with different model ensemble members depends on mean precipitation trends (Extended Data Fig. 8). For example, this relationship holds over Central Europe (correlation $\text{cor}(f_{HD}, \Delta P_{\text{mean}}) = -0.9$, Fig. 4a), where model differences and internal climate variability equally contribute to uncertainties in future f_{HD} (Fig. 2b). If mean precipitation weakly increases according to a ‘wet storyline’, compound hot–dry summers would occur in one out of ten years over Central Europe on average ($f_{HD} = 10\%$, Fig. 4d). Alternatively, an equally plausible ‘dry storyline’ characterized by decreasing mean precipitation would result in more than twice as many compound hot–dry summers ($f_{HD} = 26\%$; Fig. 4g). Future f_{HD} is also controlled by mean precipitation trends over Central North America ($\text{cor}(f_{HD}, \Delta P_{\text{mean}}) = -0.8$, Fig. 4b). According to the wet and dry storylines, regionally averaged compound-event frequencies range from 11% to 18%, respectively (Fig. 4e,h). The Amazon is a notable region where, contrary to most other regions, model differences dominate the uncertainties in precipitation trends (Extended Data Fig. 7c) and f_{HD} (Fig. 2b). As a result, for the Amazon, improving the representation of the processes dominating mean precipitation trends, particularly the plant physiological response to CO_2 ^{42,43} and changes in the Atlantic meridional overturning circulation⁴⁴,

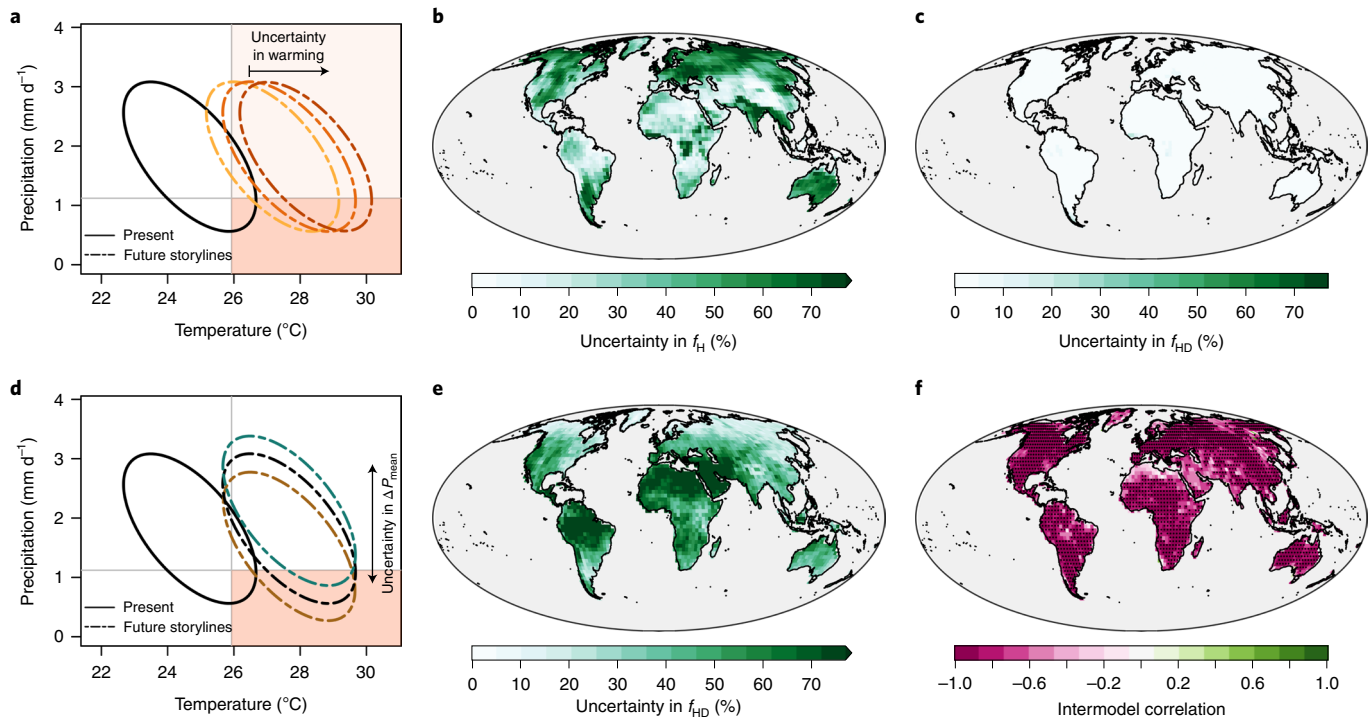


Fig. 3 | Effect of local warming and precipitation trends on the frequency of extreme events in a warmer world. **a**, Schematic illustrating the typical effect of the uncertainty in local warming trend on the future f_H (events within the right half) and f_{HD} (bottom right quadrant). Ellipses show the distribution of temperature and precipitation. The uncertainty in the local warming trend modulates the future f_H but does not affect the future f_{HD} . **b, c**, Uncertainty range in f_H (**b**) and f_{HD} (**c**) resulting from uncertainty in local warming trends (under mean projected local precipitation trends; Methods). **d**, For a given projected warming trend, the mean precipitation trend modulates the future f_{HD} . (In **a** and **d**, the colours of the future bivariate distributions represent different plausible temperature and precipitation trends, respectively.) **e**, Uncertainty range in f_{HD} resulting from uncertainty in local precipitation trends (under mean projected local warming; Methods). **f**, Intermodel correlation between the model-dependent ensemble mean of future f_{HD} and ΔP_{mean} (relative to 1950–1980; stippling indicates significance at 5% confidence level).

is essential for constraining estimates of future compound risk. Here, compound-event frequencies range from 20% to 42% (Fig. 4f,i), according to a wet and a dry storyline ($\text{cor}(f_{HD}, \Delta P_{\text{mean}}) = -0.9$, Fig. 4c).

We focused on the frequency of concurrent extremes on the basis of historical exceedance thresholds, which is a widely used indicator of the frequency of impactful compound events^{6,8–10,13,28}. The modulation of the future frequency of concurrent extremes from trends in one of the two compound-event drivers, here precipitation, is expected to hold for other compound events as long as the trends in the drivers differ strongly in magnitude (Extended Data Fig. 5). In general, the magnitude of some compound-event-related impacts may still be affected by the magnitude of exceedance in the driver with the strong trend, here temperature. Furthermore, adaptation of human and ecological systems may render historical hazard thresholds obsolete⁴⁵. However, given that many impacts are characterized by threshold behaviour in response to climate stressors, for example tree mortality², crop yields⁴⁶, heat stress in humans and other species⁴⁷, landslides⁴⁸ and floods⁴⁹, estimating compound-event frequencies on the basis of historical exceedance thresholds can be considered a suitable impact indicator^{6,9–11,13,19,31}. We thus conclude that the mechanism identified here provides relevant information to scientists and practitioners to reduce uncertainties when dealing with complex compound-event risks in the future.

Our results demonstrate that present estimates of concurrent hot and dry extremes based on relatively short climate records (<130 years) are highly uncertain as a result of internal climate variability

and thus sampling uncertainty. For future estimates, given that in a warmer climate the importance of temperature variability in determining f_{HD} uncertainties vanishes, the importance of the statistical dependence between temperature and precipitation must vanish as well. That the uncertainty in future compound-event occurrence is merely a function of uncertain precipitation trends is reflected in a strong projected reduction in the relative uncertainties of the f_{HD} (that is, $2 \times U_{IV}/f_{HD}$) that occurs despite an increase in the absolute uncertainty ($2 \times U_{IV}$) (Extended Data Fig. 9a–d). Nevertheless, relative uncertainties in the future f_{HD} due to climate model differences ($2 \times U_{MD}/f_{HD}$) increase in a warmer climate over about 75% of land masses (Extended Data Fig. 9e–h), again reflecting the need for a better understanding of forced precipitation trends. Because uncertainty in mean precipitation trends is strongly modulated by large-scale atmospheric circulation³³, our results highlight that advancing our understanding of atmospheric circulation and its change is crucial for providing stakeholders with more-robust future f_{HD} estimates. This would be especially important in case we do not meet the warming targets from the Paris Agreement because, for instance at 3 °C of global warming, model differences dominate the overall uncertainties over most land masses^{17,50} (Extended Data Fig. 10). In any case, given the difficulties in constraining large-scale atmospheric circulation^{32,33} and the omnipresent effects of internal climate variability³⁷, exploring potential impacts associated with a range of plausible storylines derived from multimodel large-ensemble simulations will offer new opportunities to develop societal preparedness for plausible worst-case scenarios.

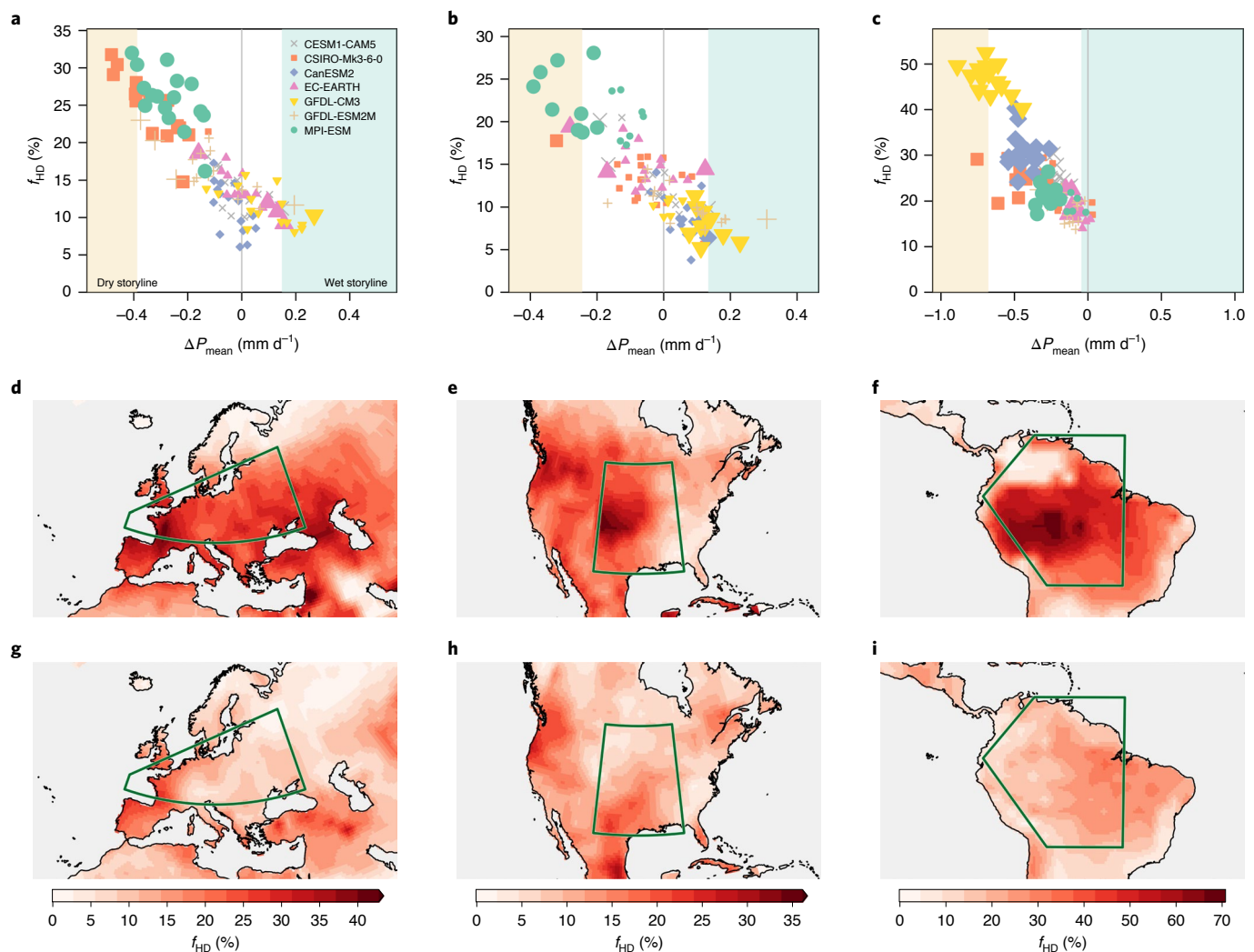


Fig. 4 | f_{HD} derived from different plausible mean precipitation trends. a–c, Regionally averaged future f_{HD} against ΔP_{mean} (relative to 1950–1980; $\Delta P_{mean, s,e}$ in Methods) for Central Europe (a), Central North America (b) and Amazon (c) from individual ensemble members of a pool of members from different climate models. Large symbols indicate changes in precipitation that are larger than internal climate variability (defined as the model-dependent 95% range of changes obtained from randomly paired present-day ensembles). Shading indicates the bottom and top 7% ensemble members in terms of regionally averaged changes in mean precipitation, that is, selected ensembles defining dry and wet storylines, respectively. **d–i**, f_{HD} spatial fields associated with dry (d–f) and wet (g–i) storylines (averages over the selected ensembles) for Central Europe (d,g), Central North America (e,h) and Amazon (f,i).

Online content

Any methods, additional references, Nature Research reporting summaries, source data, extended data, supplementary information, acknowledgements, peer review information; details of author contributions and competing interests; and statements of data and code availability are available at <https://doi.org/10.1038/s41558-022-01309-5>.

Received: 4 August 2021; Accepted: 3 February 2022;

Published online: 14 March 2022

References

- Flannigan, M. D., Krawchuk, M. A., de Groot, W. J., Wotton, B. M. & Gowman, L. M. Implications of changing climate for global wildland fire. *Int. J. Wildland Fire* **18**, 483–507 (2009).
- Allen, C. D. et al. A global overview of drought and heat-induced tree mortality reveals emerging climate change risks for forests. *For. Ecol. Manage.* **259**, 660–684 (2010).
- Zscheischler, J. et al. Impact of large-scale climate extremes on biospheric carbon fluxes: an intercomparison based on MsTMIP data. *Glob. Biogeochem. Cycles* **28**, 585–600 (2014).
- von Buttlar, J. et al. Impacts of droughts and extreme-temperature events on gross primary production and ecosystem respiration: a systematic assessment across ecosystems and climate zones. *Biogeosciences* **15**, 1293–1318 (2018).
- Ribeiro, A. F. S., Russo, A., Gouveia, C. M., Páscoa, P. & Zscheischler, J. Risk of crop failure due to compound dry and hot extremes estimated with nested copulas. *Biogeosciences* **17**, 4815–4830 (2020).
- Diffenbaugh, N. S., Swain, D. L. & Touma, D. Anthropogenic warming has increased drought risk in California. *Proc. Natl Acad. Sci. USA* **112**, 3931–3936 (2015).
- Tschumi, E. & Zscheischler, J. Countrywide climate features during recorded climate-related disasters. *Climatic Change* **158**, 593–609 (2020).
- Hao, Y., Hao, Z., Feng, S., Zhang, X. & Hao, F. Response of vegetation to El Niño–Southern Oscillation (ENSO) via compound dry and hot events in southern Africa. *Glob. Planet. Change* **195**, 103358 (2020).
- Zscheischler, J. & Seneviratne, S. I. Dependence of drivers affects risks associated with compound events. *Sci. Adv.* **3**, e1700263 (2017).
- Sarhadi, A., Ausín, M. C., Wiper, M. P., Touma, D. & Diffenbaugh, N. S. Multidimensional risk in a nonstationary climate: joint probability of increasingly severe warm and dry conditions. *Sci. Adv.* **4**, eaau3487 (2018).
- Alizadeh, M. R. et al. A century of observations reveals increasing likelihood of continental-scale compound dry–hot extremes. *Sci. Adv.* **6**, eaaz4571 (2020).

12. Manning, C. et al. Increased probability of compound long-duration dry and hot events in Europe during summer (1950–2013). *Environ. Res. Lett.* **14**, 094006 (2019).
13. Mazdiyasn, O. & AghaKouchak, A. Substantial increase in concurrent droughts and heatwaves in the United States. *Proc. Natl Acad. Sci. USA* **112**, 11484–11489 (2015).
14. Collins, M. et al. in *Climate Change 2013: The Physical Science Basis* (eds Stocker, T. F. et al.) 1029–1136 (IPCC, Cambridge Univ. Press, 2013).
15. Zappa, G., Bevacqua, E. & Shepherd, T. G. Communicating potentially large but non-robust changes in multi-model projections of future climate. *Int. J. Climatol.* **41**, 3657–3669 (2021).
16. Deser, C. et al. Insights from Earth system model initial-condition large ensembles and future prospects. *Nat. Clim. Change* **10**, 277–286 (2020).
17. Hawkins, E. & Sutton, R. The potential to narrow uncertainty in regional climate predictions. *Bull. Am. Meteorol. Soc.* **90**, 1095–1108 (2009).
18. Maher, N., Power, S. B. & Marotzke, J. More accurate quantification of model-to-model agreement in externally forced climatic responses over the coming century. *Nat. Commun.* **12**, 788 (2021).
19. Bevacqua, E. et al. Higher probability of compound flooding from precipitation and storm surge in Europe under anthropogenic climate change. *Sci. Adv.* **5**, eaaw5531 (2019).
20. Berg, A. et al. Interannual coupling between summertime surface temperature and precipitation over land: processes and implications for climate change. *J. Clim.* **28**, 1308–1328 (2015).
21. Oppenheimer, M. et al. in *Climate Change 2014: Impacts, Adaptation and Vulnerability* (eds Field, C. B. et al.) 1039–1100 (IPCC, Cambridge Univ. Press, 2015).
22. Trenberth, K. E. & Shea, D. J. Relationships between precipitation and surface temperature. *Geophys. Res. Lett.* **32**, L14703 (2005).
23. Fischer, E. M., Sedláček, J., Hawkins, E. & Knutti, R. Models agree on forced response pattern of precipitation and temperature extremes. *Geophys. Res. Lett.* **41**, 8554–8562 (2014).
24. Nishant, N. & Sherwood, S. C. How strongly are mean and extreme precipitation coupled? *Geophys. Res. Lett.* **48**, e2020GL092075 (2021).
25. Lehner, F., Deser, C. & Sanderson, B. M. Future risk of record-breaking summer temperatures and its mitigation. *Climatic Change* **146**, 363–375 (2018).
26. Perkins-Kirkpatrick, S. & Lewis, S. Increasing trends in regional heatwaves. *Nat. Commun.* **11**, 3357 (2020).
27. McKinnon, K. A., Poppick, A. & Simpson, I. R. Hot extremes have become drier in the United States Southwest. *Nat. Clim. Change* **11**, 598–604 (2021).
28. Zscheischler, J. et al. A typology of compound weather and climate events. *Nat. Rev. Earth Environ.* **1**, 333–347 (2020).
29. Le Grix, N., Zscheischler, J., Laufkötter, C., Rousseaux, C. S. & Frölicher, T. L. Compound high-temperature and low-chlorophyll extremes in the ocean over the satellite period. *Biogeosciences* **18**, 2119–2137 (2021).
30. Chen, Y., Liao, Z., Shi, Y., Tian, Y. & Zhai, P. Detectable increases in sequential flood–heatwave events across China during 1961–2018. *Geophys. Res. Lett.* **48**, e2021GL092549 (2021).
31. Matthews, T., Wilby, R. L. & Murphy, C. An emerging tropical cyclone–deadly heat compound hazard. *Nat. Clim. Change* **9**, 602–606 (2019).
32. Shepherd, T. G. Atmospheric circulation as a source of uncertainty in climate change projections. *Nat. Geosci.* **7**, 703–708 (2014).
33. Zappa, G. Regional climate impacts of future changes in the mid-latitude atmospheric circulation: a storyline view. *Curr. Clim. Change Rep.* **5**, 358–371 (2019).
34. Simpson, I. R., Seager, R., Ting, M. & Shaw, T. A. Causes of change in Northern Hemisphere winter meridional winds and regional hydroclimate. *Nat. Clim. Change* **6**, 65–70 (2016).
35. Vogel, M. M., Zscheischler, J. & Seneviratne, S. I. Varying soil moisture–atmosphere feedbacks explain divergent temperature extremes and precipitation projections in central Europe. *Earth Syst. Dyn.* **9**, 1107–1125 (2018).
36. Padrón, R. S., Gudmundsson, L. & Seneviratne, S. I. Observational constraints reduce likelihood of extreme changes in multidecadal land water availability. *Geophys. Res. Lett.* **46**, 736–744 (2019).
37. Deser, C. Certain uncertainty: the role of internal climate variability in projections of regional climate change and risk management. *Earth's Future* **8**, e2020EF001854 (2020).
38. Shepherd, T. G. Storyline approach to the construction of regional climate change information. *Proc. R. Soc. A* **475**, 20190013 (2019).
39. Zappa, G. & Shepherd, T. G. Storylines of atmospheric circulation change for European regional climate impact assessment. *J. Clim.* **30**, 6561–6577 (2017).
40. Bevacqua, E., Zappa, G. & Shepherd, T. G. Shorter cyclone clusters modulate changes in European wintertime precipitation extremes. *Environ. Res. Lett.* <https://doi.org/10.1088/1748-9326/abbde7> (2020).
41. Mindlin, J. et al. Storyline description of Southern Hemisphere midlatitude circulation and precipitation response to greenhouse gas forcing. *Clim. Dyn.* **54**, 4399–4421 (2020).
42. Kooperman, G. J. et al. Forest response to rising CO₂ drives zonally asymmetric rainfall change over tropical land. *Nat. Clim. Change* **8**, 434–440 (2018).
43. Saint-Lu, M., Chadwick, R., Lambert, F. H. & Collins, M. Surface warming and atmospheric circulation dominate rainfall changes over tropical rainforests under global warming. *Geophys. Res. Lett.* **46**, 13410–13419 (2019).
44. Chen, Y., Langenbrunner, B. & Randerson, J. T. Future drying in Central America and northern South America linked with Atlantic meridional overturning circulation. *Geophys. Res. Lett.* **45**, 9226–9235 (2018).
45. Vogel, M. M., Zscheischler, J., Fischer, E. M. & Seneviratne, S. I. Development of future heatwaves for different hazard thresholds. *J. Geophys. Res. Atmos.* **125**, e2019JD032070 (2020).
46. Troy, T. J., Kipgen, C. & Pal, I. The impact of climate extremes and irrigation on US crop yields. *Environ. Res. Lett.* **10**, 054013 (2015).
47. Asseng, S., Spänkuch, D., Hernandez-Ochoa, I. M. & Laporta, J. The upper temperature thresholds of life. *Lancet Planet. Health* **5**, e378–e385 (2021).
48. Guzzetti, F., Peruccacci, S., Rossi, M. & Stark, C. P. Rainfall thresholds for the initiation of landslides in central and southern Europe. *Meteorol. Atmos. Phys.* **98**, 239–267 (2007).
49. van den Hurk, B., van Meijgaard, E., de Valk, P., van Heeringen, K.-J. & Gooijer, J. Analysis of a compounding surge and precipitation event in the Netherlands. *Environ. Res. Lett.* **10**, 035001 (2015).
50. Lehner, F. et al. Partitioning climate projection uncertainty with multiple large ensembles and CMIP5/6. *Earth Syst. Dyn.* **11**, 491–508 (2020).

Publisher's note Springer Nature remains neutral with regard to jurisdictional claims in published maps and institutional affiliations.



Open Access This article is licensed under a Creative Commons Attribution 4.0 International License, which permits use, sharing, adaptation, distribution and reproduction in any medium or format, as long as you give appropriate credit to the original author(s) and the source, provide a link to the Creative Commons license, and indicate if changes were made. The images or other third party material in this article are included in the article's Creative Commons license, unless indicated otherwise in a credit line to the material. If material is not included in the article's Creative Commons license and your intended use is not permitted by statutory regulation or exceeds the permitted use, you will need to obtain permission directly from the copyright holder. To view a copy of this license, visit <http://creativecommons.org/licenses/by/4.0/>.

© The Author(s) 2022

Methods

Data. We used seven SMILES: CESM1-CAM5⁵¹ (including 40 ensemble members), CSIRO-Mk3-6-0⁵² (30), CanESM2⁵³ (50), EC-EARTH⁵⁴ (16), GFDL-CM3⁵⁵ (20), GFDL-ESM2M⁵⁶ (30) and MPI-ESM⁵⁷ (100). Monthly temperature and precipitation data were available for all models for the period 1950–2099, based on the representative concentration pathway⁵⁸ RCP8.5 after 2005. Soil moisture over the total column (employed in Extended Data Fig. 4e,f) was available likewise, but only for models CESM1-CAM5, CSIRO-Mk3-6-0, GFDL-CM3 and MPI-ESM. We considered 1950–1980 as the historical baseline period. The considered historical period has a length of 31 years, similar to the length routinely used in climate studies. Considering a shorter or longer period would result in a higher and lower uncertainty due to internal climate variability, hence a decrease and increase of the uncertainty in the frequency of compound hot–dry events due to model-to-model differences relative to the full uncertainty range, respectively. However, considering a period of a different length would not affect the main conclusions of the study.

For each model, to obtain model data in a world 2°C (or 3°C, considered in Extended Data Fig. 10 only) warmer than pre-industrial conditions in 1870–1900, we selected the earliest 31 yr time window in which the average global warming relative to 1950–1980 is higher than 2°C (or 3°C) minus the observed warming from 1870–1900 to 1950–1980 (about 0.28°C on the basis of observations from the HadCRUT5 dataset⁵⁹). Model data were bilinearly interpolated to an equal 2.5° spatial grid before all calculations (for graphical purposes, the fields in Figs. 1 and 4 were interpolated to a finer grid at the end of the analysis).

Definition of compound hot–dry events. Following ref. ⁹, our analysis focuses on land (excluding Antarctica) and on temperature and precipitation mean values over the warm season, that is, the average hottest three consecutive months during 1950–1980 (we also consider the average wettest three consecutive months in Extended Data Fig. 4c,d). Considering three months' mean values is a compromise between the longer timescales of droughts (which may last even three months and more) and the shorter timescales of heatwaves (several days)⁹ and generally provide a good indicator of summertime impacts^{60,61}. Overall, choosing different timescales leads to similar spatial patterns in the frequency of compound events⁶².

We compute empirical frequencies of concurrent extremes (f_{HD}) and univariate extremes. For each model, extreme events of mean temperature and precipitation were defined as values above the 90th percentile and below the 10th percentile, respectively, of the distribution obtained by pooling together data of the period 1950–1980 from all available ensemble members (hence, extreme events in a warmer climate are defined on the basis of historical percentile thresholds). Employing more extreme percentiles to define extreme events would imply the considered compound events are very rare in the historical period; for example, the global average of f_{HD} over land is 0.14% (corresponding to compound events occurring every 713 years on average) when employing the 99th and 1st percentile thresholds for defining temperature and precipitation extremes, respectively. We confirm that our main result, that precipitation trends determine future occurrences of compound hot–dry events, generally holds when employing more extreme thresholds than the historical 10th and 90th percentiles (for example, for 5th and 95th percentiles, Extended Data Fig. 4a,b). This is in line with the fact that most future droughts (precipitation lower than the 5th percentile) are hot (temperature higher than the 95th percentile) for 94% of droughts on average over land masses (multimodel mean value). Similarly, 89% of droughts are hot when employing 1st and 99th percentiles to define precipitation and temperature extremes, respectively, and 83% of droughts are hot when employing the 10th and 99th percentiles to define precipitation and temperature extremes, respectively.

Note that the analysis of compound hot–dry events defined on the basis of soil moisture (Extended Data Fig. 4e,f) rather than on precipitation, that is, on the basis of dry events associated with soil moisture drought rather than meteorological drought, was carried out exactly as the analysis based on temperature and precipitation, but swapping precipitation for soil moisture and employing only four climate models.

Calculation of ensemble mean, multimodel mean, U_{IV} and U_{MD} . Following ref. ¹⁸, given a statistical quantity of interest X , we quantified the contribution to its uncertainty from uncertainty due to internal climate variability (U_{IV}) and model differences (U_{MD}). Here, X can be the f_{HD} in the historical or future period, the historical frequency of hot events f_H , the projected change in mean precipitation ΔP_{mean} , or the projected change in mean temperature ΔT_{mean} . U_{MD} and U_{IV} were obtained starting from $X_{s,e}$, which is the estimate of the statistical quantity X in the ensemble member e of the SMILE model s . That is, when interested in the uncertainty of f_{HD} in the historical period, $X_{s,e} = f_{HD}^{hist, s,e}$ (analogously for the future f_{HD} and for the historical f_H). When interested in ΔP_{mean} , $X_{s,e} = \Delta P_{mean, s,e}$, we computed $\Delta P_{mean, s,e} = P_{mean, s,e}^{fut} - P_{mean, s,e}^{hist}$, where $P_{mean, s,e}^{fut}$ is the mean precipitation in the future scenario (analogously for the change in mean temperature).

The mean value of X in any single SMILE (s) was calculated as the model-dependent ensemble mean:

$$X_{s,\bar{e}} = \frac{1}{N_s} \sum_{e=1}^{N_s} X_{s,e} \quad (1)$$

where N_s is the ensemble size of the considered SMILE model s . $X_{s,\bar{e}}$ represents an estimate of the quantity X in the considered SMILE, where averaging across the ensemble members (indicated as \bar{e}) leads to filtering out variations due to internal climate variability. When the quantity of interest X is a projected change, for example, ΔP_{mean} , it represents the forced response of P_{mean} in the considered SMILE. The multimodel mean of X based on the $N^{mod} = 7$ SMILES was computed as the mean across the individual SMILE ensemble means:

$$X_{\bar{s},\bar{e}} = \frac{1}{N^{mod}} \sum_{s=1}^{N^{mod}} X_{s,\bar{e}}. \quad (2)$$

The uncertainty in X in a single realization due to internal climate variability (that is, in practice, the uncertainty in the quantity X , when X is estimated from a single ensemble member of a given model) was estimated as an average of the internal climate variability effect on X in the seven SMILES:

$$U_{IV} = \sqrt{\frac{1}{N^{mod}} \sum_{s=1}^{N^{mod}} \sigma^2(X_s)} \quad (3)$$

where, in the SMILE s , the spread in X due to internal climate variability was calculated as the sample standard deviation of X across the ensemble members:

$$\sigma(X_s) = \sqrt{\frac{1}{N_s - 1} \sum_{e=1}^{N_s} (X_{s,e} - X_{s,\bar{e}})^2}. \quad (4)$$

Note that given that U_{IV} is obtained on the basis of the standard deviation, the value $2 \times U_{IV}$ employed in Fig. 1c provides an estimate of the 68.2% uncertainty range in X due to internal climate variability (assuming that X is normally distributed—note that the actual distribution may deviate from normality; however, we tested that $2 \times U_{IV}$ is similar when employing a quantile-based estimate of the standard deviation in equation (3)).

The uncertainty in X due to model differences (in practice, the uncertainty in the quantity X , when X is estimated on the basis of a single SMILE, that is, on the basis of large-ensemble simulations from a single model) was quantified as the square root of the variance of the ensemble mean of X in the seven SMILES. In practice, we first calculated:

$$\sigma_{MD}^2 = D^2 - E^2 \quad (5)$$

where D^2 is the sample variance of the ensemble means:

$$D^2 = \frac{1}{N^{mod} - 1} \sum_{s=1}^{N^{mod}} (X_{s,\bar{e}} - X_{\bar{s},\bar{e}})^2 \quad (6)$$

and E^2 is a correction term that accounts for the inflation of the variance of the ensemble means due to internal climate variability⁶³, which is equal to

$$E^2 = \frac{1}{N^{mod}} \sum_{s=1}^{N^{mod}} \frac{\sigma^2(X_s)}{N_s}. \quad (7)$$

The larger the ensemble size, the smaller this correction term becomes¹⁸. In a few locations where model differences are small, it can occur that $D^2 - E^2 < 0$, resulting in U_{MD} not being defined. In these cases, we set $E^2 = 0$. Finally, the uncertainty in X due to model differences was quantified as:

$$U_{MD} = \sqrt{\sigma_{MD}^2}. \quad (8)$$

Dependence of U_{IV} on sample size. We estimated how sample size affects the U_{IV} of both f_{HD} and f_H in the historical period. To achieve this, we created bootstrapped ensemble members of varying sample sizes (N^{years}) from the 31 yr historical period (1950–1980) of MPI-ESM, the model with the largest number of ensemble members (100). Specifically, for any N^{years} of interest, we constructed 12 ensemble members with sample size of N^{years} years through sampling without replacement from the pool of $31 \times 100 = 3,100$ years of data. We consider 12 ensemble members as it allows for exploring uncertainties associated with a large sample size. In fact, using the 3,100 available years, the procedure allows for constructing 12 independent ensemble members having a sample size up to 258 years. On the basis of the 12 ensemble members, we computed the relative uncertainty $2 \times U_{IV}/f_{HD}$, where f_{HD} was obtained via equation (1) and the uncertainty due to internal climate variability via equation (3), which—given that only one model is considered here—corresponds to the sample standard deviation of f_{HD} across the 12 ensemble members (analogously for the f_H). Hereby, N^{years} varies from 15 to 258 years. Note that results for f_H and for the frequency of dry events are virtually identical; therefore, only f_H is shown in Extended Data Fig. 1b.

We tested that 12 ensemble members are enough for studying relative uncertainties. Results are robust to the random sampling; that is, the results are virtually identical when repeating the analysis multiple times. Combining annual data from different ensemble members is acceptable given that serial correlations of temperature and precipitation are very low on land areas⁹. Overall, this method based on 12 randomly generated ensemble members from a single model (MPI-ESM) provides a robust estimate of the effect of internal variability, as demonstrated by the nearly identical uncertainty values obtained via the preceding method and that used in the rest of the paper for $N^{\text{ens}} = 31$ years (see coloured dots in Extended Data Fig. 1b).

Area-weighted aggregated statistics. All the statistics, such as mean, quantiles and percentage of land masses, were weighted on the basis of the gridpoints surfaces, employing the R packages `wCorr`⁶⁴ and `spatstat`⁶⁵.

Pool of randomly sampled ensemble members. To obtain the composite maps in Fig. 1d–i and the plots in Fig. 4 and Extended Data Fig. 8, and to carry out the experiments introduced in the next three sections, we consider a pool of randomly sampled ensemble members from the merged members of all climate models. To give the same weight to all models, each model contributes equally to the pool with 16 randomly sampled members, where 16 is the number of available ensemble members from the climate model with the lowest number of members.

Uncertainty range from uncertainty in local mean warming and precipitation trends. We performed two experiments (results shown in Fig. 3) to quantify (1) the uncertainty range in the future f_{HD} (similarly for the f_{H}) arising from the uncertainty in the change of local mean temperature, that is, uncertainty in local temperature trends, and (2) the uncertainty range in the future f_{HD} arising from the uncertainty in the change of local mean precipitation, that is, uncertainty in local precipitation trends.

At a given location, as a first step, we defined a wide range of plausible changes of mean precipitation and temperature. That is, from the pool of ensemble members introduced in the preceding section, we defined the highest, average, and lowest change of mean precipitation ($\Delta P_{\text{mean}}^{\text{high}}$, $\Delta P_{\text{mean}}^{\text{average}}$ and $\Delta P_{\text{mean}}^{\text{low}}$) and temperature ($\Delta T_{\text{mean}}^{\text{high}}$, $\Delta T_{\text{mean}}^{\text{average}}$ and $\Delta T_{\text{mean}}^{\text{low}}$). These values are used in the two experiments as follows.

In experiment (1), we computed the difference between f_{HD} (analogously for f_{H}) resulting from two scenarios that combine the estimated mean future precipitation with $\Delta T_{\text{mean}}^{\text{high}}$ and $\Delta T_{\text{mean}}^{\text{low}}$. Specifically, for a given SMILE model s , we compute the difference in f_{HD} (analogously for f_{H}) associated with the bivariate data ($T_s^{\text{hist}} + \Delta T_{\text{mean}}^{\text{high}}$, $P_s^{\text{hist}} + \Delta P_{\text{mean}}^{\text{average}}$) and ($T_s^{\text{hist}} + \Delta T_{\text{mean}}^{\text{low}}$, $P_s^{\text{hist}} + \Delta P_{\text{mean}}^{\text{average}}$), where T_s^{hist} and P_s^{hist} are the historical data of the SMILE model s (data of the period 1950–1980; T_s^{hist} and P_s^{hist} are obtained by merging data from all ensemble members of the SMILE model s such as to get a unique reference dataset and more-robust estimates). Finally, we defined the uncertainty range as the multimodel mean of the preceding difference.

We conducted experiment (2) as experiment (1), but we computed the difference between the highest and lowest f_{HD} associated with the bivariate data ($T_s^{\text{hist}} + \Delta T_{\text{mean}}^{\text{average}}$, $P_s^{\text{hist}} + \Delta P_{\text{mean}}^{\text{low}}$) and ($T_s^{\text{hist}} + \Delta T_{\text{mean}}^{\text{average}}$, $P_s^{\text{hist}} + \Delta P_{\text{mean}}^{\text{high}}$).

Uncertainty range in f_{HD} for different combinations of mean warming and precipitation trends. The uncertainty range in the future f_{HD} is controlled by the uncertainty in precipitation and is not affected by uncertainty in the local warming (Fig. 3). To demonstrate that this results mainly from expected changes in mean temperature being much larger than expected changes in mean precipitation, we carried out, in line with the procedure of the preceding section, two idealized experiments (results shown in Extended Data Fig. 3). In the two experiments, we quantified, for different combinations of expected changes in mean temperature and precipitation, the uncertainty range in the future f_{HD} arising (experiment 1) from the uncertainty in the change of local mean temperature (that is, uncertainty in local temperature trends), and (experiment 2) from the uncertainty in the change of local mean precipitation (that is, uncertainty in local precipitation trends).

We first defined the uncertainty in mean temperature change $\sigma_{\Delta T}$ (analogously for precipitation, $\sigma_{\Delta P}$) as the global median of the location-dependent standard deviation of changes in temperature from the pool of ensemble members introduced in the preceding section (Pool of randomly sampled ensemble members). (Note that while $\sigma_{\Delta T}$ and $\sigma_{\Delta P}$ can be different for different expected changes in mean temperature and precipitation, for example, under different scenarios of global warming, we kept them constant in this idealized experiment, which allows for disentangling the individual effect of differences in expected changes in mean temperature and precipitation on f_{HD} uncertainty.) The values $\sigma_{\Delta T}$ and $\sigma_{\Delta P}$ are then used in the two experiments as follows.

In experiment (1), the values are used to quantify, for different combinations of expected changes in mean temperature and precipitation, the uncertainty range in the future f_{HD} arising from the uncertainty in the change of local mean temperature. For a given combination of expected changes in mean temperature (ΔT_{mean}) and precipitation (ΔP_{mean}), we defined the uncertainty range in f_{HD} as the difference between the highest and lowest f_{HD} resulting from two divergent scenarios associated with two diverging local mean temperature changes.

That is, we compute the difference in f_{HD} associated with two bivariate Gaussian distributions (approximating the temperature–precipitation distribution) whose means are $(T_{\text{mean}}^{\text{fut}} \pm 2 \times \sigma_{\Delta T}, P_{\text{mean}}^{\text{fut}})$, where $T_{\text{mean}}^{\text{fut}} = T_{\text{mean}}^{\text{hist}} + \Delta T_{\text{mean}}$ and $T_{\text{mean}}^{\text{hist}}$ is the mean temperature in the historical period (analogously for precipitation). (Note that in Extended Data Fig. 3, we also show with contours the f_{HD} associated with the bivariate Gaussian distribution whose means are $(T_{\text{mean}}^{\text{fut}}, P_{\text{mean}}^{\text{fut}})$, which aids further interpretation of Fig. 2 discussed in the Supplementary Information.)

In experiment (2), the values are used to quantify, for different combinations of expected changes in mean temperature and precipitation, the uncertainty range in the future f_{HD} arising from the uncertainty in the change of local mean precipitation. This is as in experiment (1), but we computed the difference between the f_{HD} associated with two bivariate Gaussian distributions whose means are $(T_{\text{mean}}^{\text{fut}}, P_{\text{mean}}^{\text{fut}} \pm 2 \times \sigma_{\Delta P})$.

In all experiments, we considered realistic standard deviations (and mean values) of precipitation and temperature for the Gaussian distribution (we employ the distribution of Fig. 3a; note that results are independent of the marginal distribution mean values and that results are shown also in units of standard deviations to allow for a better comparison of the behaviour at locations with different present-day standard deviations; Extended Data Fig. 3). Both the preceding experiments were repeated three times, considering a Gaussian distribution with correlation between precipitation and temperature $\text{cor}(T, P) = -0.5$, which is in line with observed values during the warm season considered here⁹, $\text{cor}(T, P) = 0$ and $\text{cor}(T, P) = 0.5$.

Correlation between variability in the future f_{HD} and temperature and precipitation trends. The future f_{HD} is correlated with precipitation trends; that is, models (or ensemble members) that project a stronger increase in mean precipitation lead to a lower future f_{HD} , and vice versa (Figs. 3f and 4). To demonstrate that this result stems mainly from expected changes in mean temperature being much larger than expected changes in mean precipitation, and how the underlying negative dependence between temperature and precipitation affects the preceding, we carried out an idealized experiment (results shown in Extended Data Fig. 5).

For a combination of different expected ΔT_{mean} and ΔP_{mean} , we quantified the correlation between the variability around such changes and the future f_{HD} . Specifically, for a given combination of ΔT_{mean} and ΔP_{mean} , we obtain 1,000 pairs of future f_{HD} and variability around the expected ΔT_{mean} (analogously for ΔP_{mean}), which are used to compute the correlation. To obtain each of the 1,000 pairs, we simulated 300 pairs of temperature and precipitation from a bivariate Gaussian distribution (with $\text{cor}(T, P) = -0.5, 0$ and 0.5 and the same standard deviations as in the preceding experiment). We prescribed the mean of the distribution as $(T_{\text{mean}}^{\text{fut}}, P_{\text{mean}}^{\text{fut}})$, where $T_{\text{mean}}^{\text{fut}} = T_{\text{mean}}^{\text{hist}} + \Delta T_{\text{mean}}$ and $T_{\text{mean}}^{\text{hist}}$ is the mean temperature in the historical period (analogously for precipitation). The variability around the expected ΔT_{mean} and ΔP_{mean} was obtained on the basis of $\sigma_{\Delta T}$ and $\sigma_{\Delta P}$, which were defined as in the preceding section to resemble the uncertainty around the expected changes. That is, normally distributed noise $\eta_T \sim \mathcal{N}(0, \sigma_{\Delta T})$ and $\eta_P \sim \mathcal{N}(0, \sigma_{\Delta P})$ is added to the 1,000 simulated $T_{\text{mean}}^{\text{fut}}$ and $P_{\text{mean}}^{\text{fut}}$. We then compute f_{HD} for the i -th 1,000 simulations, which is finally used to compute the correlation of the 1,000 pairs (f_{HD}, η_T) and (f_{HD}, η_P) .

Finally, we note that considering a bivariate Gaussian distribution is acceptable for seasonal values of precipitation and temperature and allows for a simple understanding of the mechanism under investigation and how it may affect the dynamic of other compound events. Seasonal precipitation may have a skewed distribution in some areas; hence, we tested that the results are qualitatively similar when considering a bivariate distribution such as the Gaussian but with a Gamma distribution for precipitation values (that is, combining⁶⁶ a Gaussian copula with a Gaussian marginal distribution for temperature and a Gamma distribution for precipitation).

Regional storylines of future f_{HD} . In Fig. 4a, we show plausible storylines of future f_{HD} resulting from two contrasting precipitation trends. That is, for a given region, we build the dry storyline of future f_{HD} through averaging f_{HD} spatial fields associated with the bottom 7% ensemble members of a pool of members in terms of regionally averaged changes in mean precipitation. The same approach is taken to create a wet storyline, which corresponds to the top 7% ensemble members. The pool of ensemble members is introduced in the section ‘Pool of randomly sampled ensemble members’.

Data availability

The model data used in the study are openly available online at <https://esgf-data.dkrz.de/projects/mipi-ge/> (for the model MPI-GE) and https://www.earthsystemgrid.org/dataset/ucar.cgd.cesm4.CLIVAR_LE.html (for the other models: CanESM2, CESM-LE, CSIRO-Mk3-6-0, GFDL-ESM2M and GFDL-CM3). The HadCRUT5 dataset is available at <https://www.metoffice.gov.uk/hadobs/hadcrut5/>.

Code availability

All custom codes are direct implementations of standard methods and techniques, described in detail in Methods.

References

51. Kay, J. E. et al. The Community Earth System Model (CESM) large ensemble project: a community resource for studying climate change in the presence of internal climate variability. *Bull. Am. Meteorol. Soc.* **96**, 1333–1349 (2015).
52. Jeffrey, S. et al. Australia's CMIP5 submission using the CSIRO-Mk3.6 model. *Aust. Meteorol. Oceanogr.* **63**, 1–13 (2013).
53. Kirchmeier-Young, M. C., Zwiers, F. W. & Gillett, N. P. Attribution of extreme events in Arctic sea ice extent. *J. Clim.* **30**, 553–571 (2017).
54. Hazeleger, W. et al. EC-Earth: a seamless Earth-system prediction approach in action. *Bull. Am. Meteorol. Soc.* **91**, 1357–1363 (2010).
55. Sun, L., Alexander, M. & Deser, C. Evolution of the global coupled climate response to Arctic sea ice loss during 1990–2090 and its contribution to climate change. *J. Clim.* **31**, 7823–7843 (2018).
56. Rodgers, K. B., Lin, J. & Frölicher, T. L. Emergence of multiple ocean ecosystem drivers in a large ensemble suite with an Earth system model. *Biogeosciences* **12**, 3301–3320 (2015).
57. Maher, N. et al. The Max Planck Institute Grand Ensemble: enabling the exploration of climate system variability. *J. Adv. Model. Earth Syst.* **11**, 2050–2069 (2019).
58. Moss, R. H. et al. The next generation of scenarios for climate change research and assessment. *Nature* **463**, 747–756 (2010).
59. Morice, C. P. et al. An updated assessment of near-surface temperature change from 1850: the HadCRUT5 dataset. *J. Geophys. Res. Atmos.* **126**, e2019JD032361 (2020).
60. Orth, R., Zscheischler, J. & Seneviratne, S. I. Record dry summer in 2015 challenges precipitation projections in Central Europe. *Sci. Rep.* **6**, 28334 (2016).
61. Bastos, A. et al. Direct and seasonal legacy effects of the 2018 heat wave and drought on European ecosystem productivity. *Sci. Adv.* **6**, eaba2724 (2020).
62. Brunner, M. I., Gilleland, E. & Wood, A. W. Space–time dependence of compound hot–dry events in the United States: assessment using a multi-site multi-variable weather generator. *Earth Syst. Dyn.* **12**, 621–634 (2021).
63. Rowell, D. P., Folland, C. K., Maskell, K. & Ward, M. N. Variability of summer rainfall over tropical North Africa (1906–92): observations and modelling. *Q. J. R. Meteorol. Soc.* **121**, 669–704 (1995).
64. Emad, A. & Bailey, P. wCorr: Weighted Correlations. R package v.1.9.1 <https://cran.r-project.org/web/packages/wCorr/index.html> (2017).
65. Baddeley, A. J. & Turner, R. Spatstat: an R package for analyzing spatial point patterns. *J. Stat. Softw.* <https://doi.org/10.18637/jss.v012.i06> (2005).
66. Bevacqua, E., Maraun, D., Hobæk Haff, I., Widmann, M. & Vrac, M. Multivariate statistical modelling of compound events via pair-copula constructions: analysis of floods in Ravenna (Italy). *Hydrol. Earth Syst. Sci.* **21**, 2701–2723 (2017).

Acknowledgements

We acknowledge the European COST Action DAMOCLES (CA17109). This project has received funding from the European Union's Horizon 2020 research and innovation programme under grant agreement no. 101003469. G.Z. acknowledges financial support from the ERA4CS-MEDSCOPE project (grant agreement 690462), co-funded by the Horizon 2020 Framework Program of the European Union. F.L. was supported by the Regional and Global Model Analysis (RGMA) component of the Earth and Environmental System Modeling Program of the US Department of Energy's Office of Biological & Environmental Research (BER) Cooperative Agreement DE-FC02-97ER62402. J.Z. acknowledges the Swiss National Science Foundation (Ambizione grant 179876) and the Helmholtz Initiative and Networking Fund (Young Investigator Group COMPOUNDX; grant agreement no. VH-NG-1537). We thank the US CLIVAR Working Group on Large Ensembles and NSF AGS-0856145 Amendment 87 for supporting the Multi-Model Large Ensemble Archive. We also thank the modelling centres for providing the simulations.

Author contributions

E.B. and J.Z. initiated and designed the study. E.B. carried out the analysis. E.B. wrote the manuscript with contributions from J.Z. All authors (E.B., G.Z., F.L. and J.Z.) discussed the results and reviewed the manuscript.

Funding

Open access funding provided by Helmholtz-Zentrum für Umweltforschung GmbH - UFZ.

Competing interests

The authors declare no competing interests.

Additional information

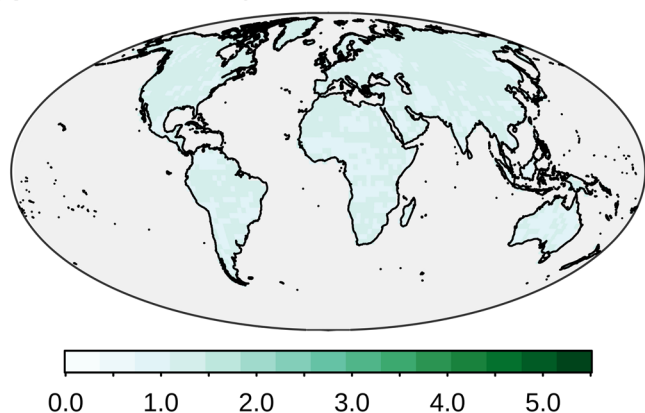
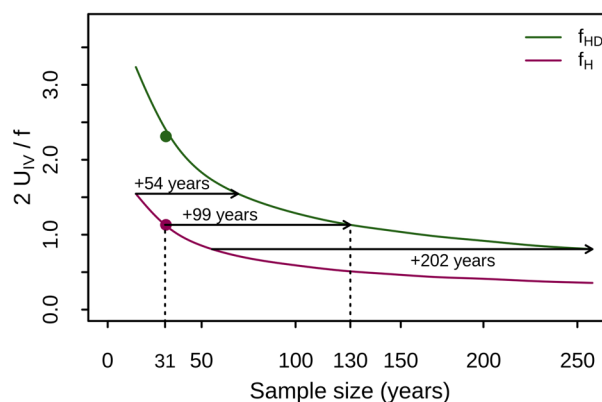
Extended data is available for this paper at <https://doi.org/10.1038/s41558-022-01309-5>.

Supplementary information The online version contains supplementary material available at <https://doi.org/10.1038/s41558-022-01309-5>.

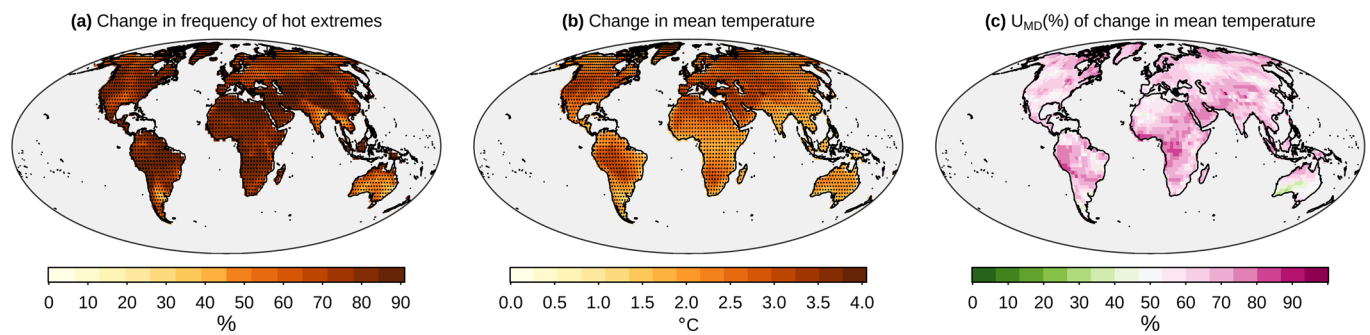
Correspondence and requests for materials should be addressed to Emanuele Bevacqua.

Peer review information *Nature Climate Change* thanks Vimal Mishra, Ameneh Tavakol and the other, anonymous, reviewer(s) for their contribution to the peer review of this work.

Reprints and permissions information is available at www.nature.com/reprints.

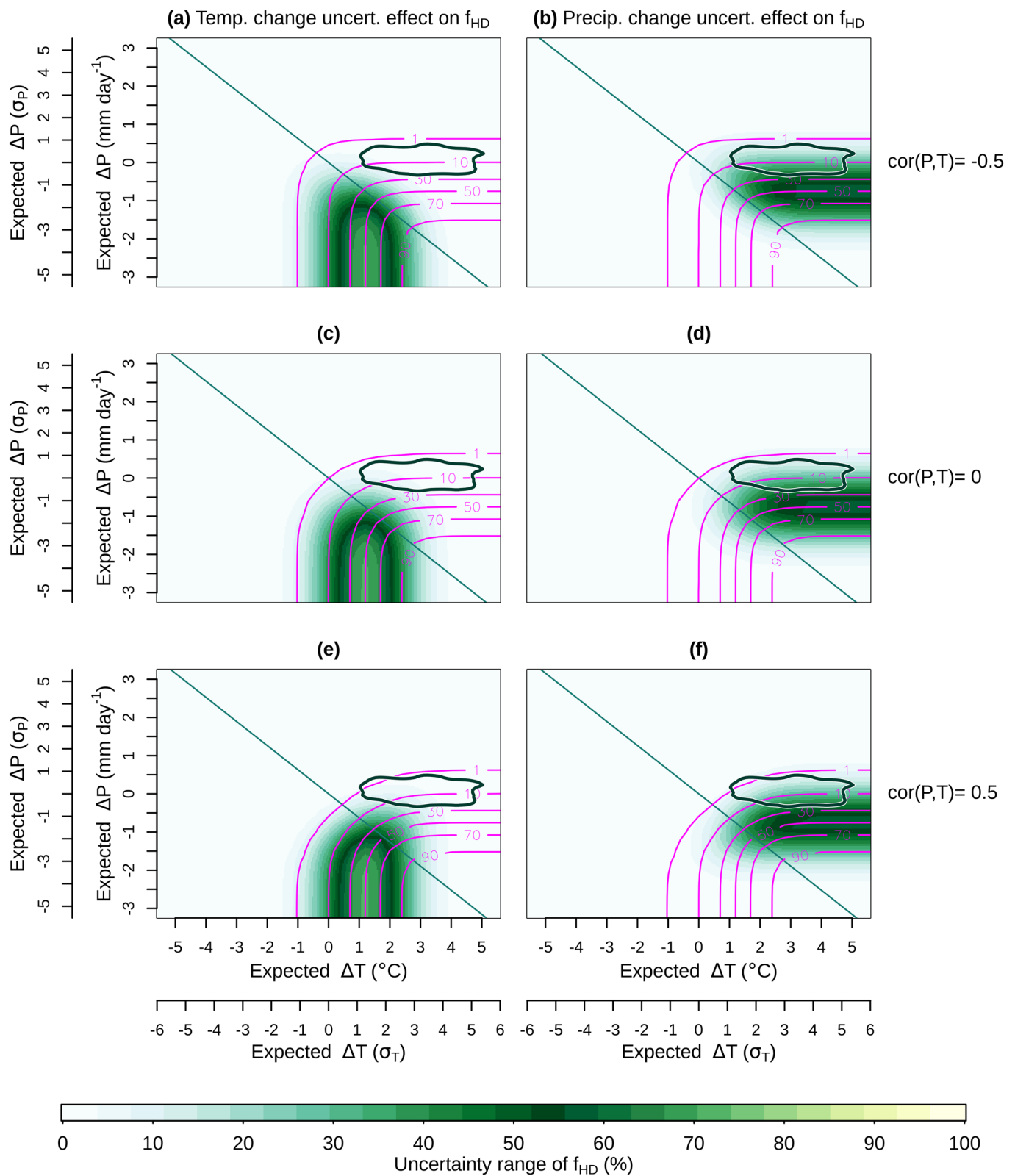
(a) Relative uncertainty in f_H from internal climate variability**(b)** Dependence of relative uncertainty on sample size

Extended Data Fig. 1 | Relative uncertainty due to internal climate variability in frequencies of hot events (f_H) and compound hot-dry events (f_{HD}) in the historical period. **a, The same as Fig. 1c, but for f_H , that is the uncertainty in f_H due to internal climate variability ($2 \times U_{IV}$) relative to f_H . The image is obtained using, as in the rest of the paper, samples of 31 years. The same palette as in Fig. 1c is used for comparison. **b**, Curves show the dependence of the relative uncertainty due to internal climate variability in f_{HD} (green) and f_H (magenta) on the sample size. To explore the relationship for large sample sizes, the curves are obtained based on a method that employs data from the model with the largest number of ensembles, that is the MPI-ESM model (Methods). The arrows indicate the difference between the sample size required to obtain fixed levels of relative uncertainty for f_{HD} and f_H . The green and magenta dots show the relative uncertainties obtained via the method used in the rest of the paper, hence based on all seven climate models and 31 years of data. The match between the dots and the curve highlights that the estimate of the uncertainty obtained through the MPI-ESM-based method provides accurate information.**



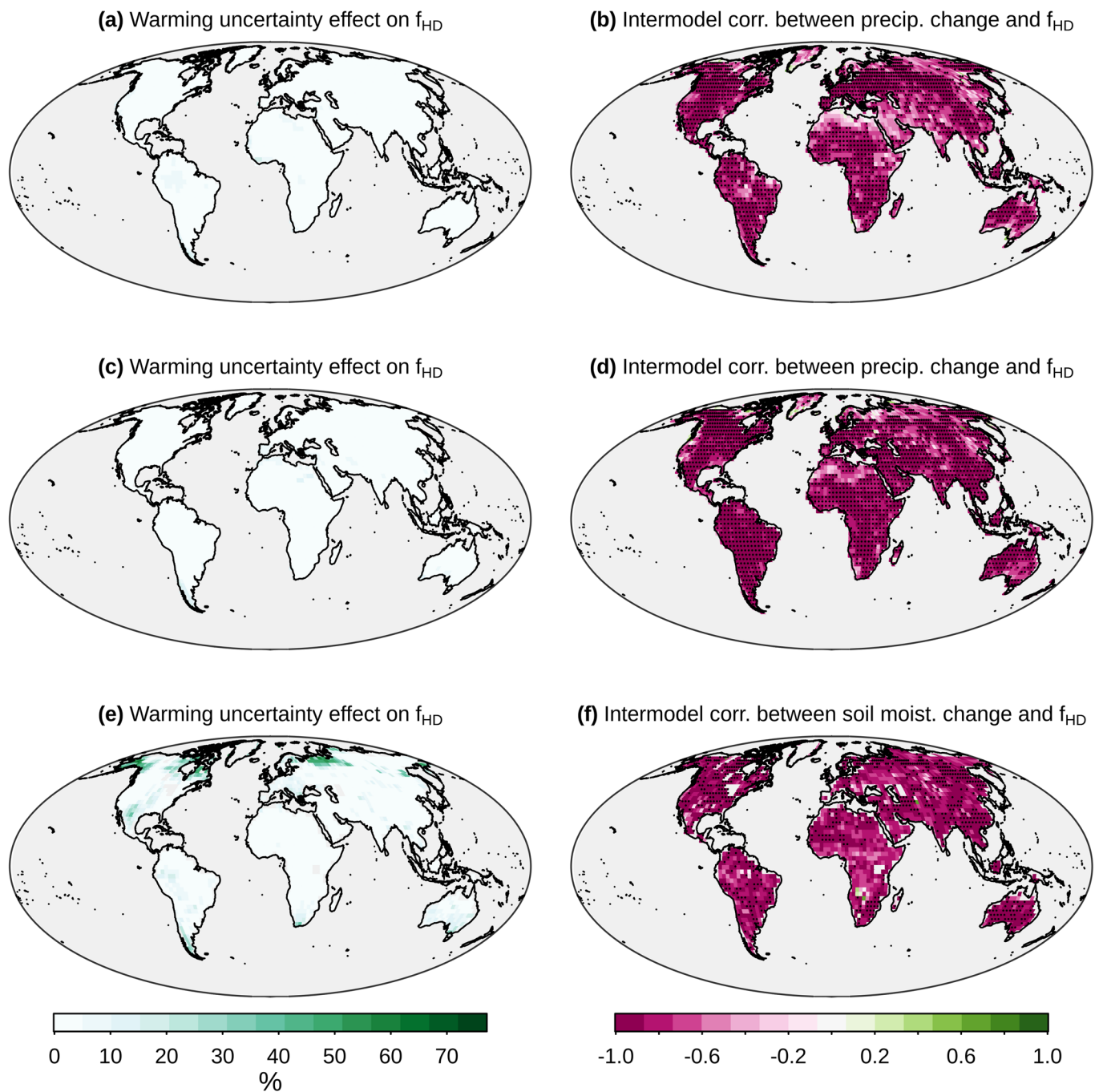
Extended Data Fig. 2 | Temperature changes in a world 2 °C warmer than pre-industrial conditions and associated drivers of uncertainties.

a, Multimodel mean projected change in frequency of hot extreme events (relative to 1950–1980). Stippling indicates locations where at least six out of seven models agree on the sign of the change. **b**, As in panel **a**, but for changes in mean temperature. **c**, Uncertainty in the change in mean temperature due to model-to-model differences (U_{MD}) relative to the sum of U_{IV} (uncertainty due to internal climate variability) and U_{MD} (expressed in percentage; see Methods).



Extended Data Fig. 3 | See next page for caption.

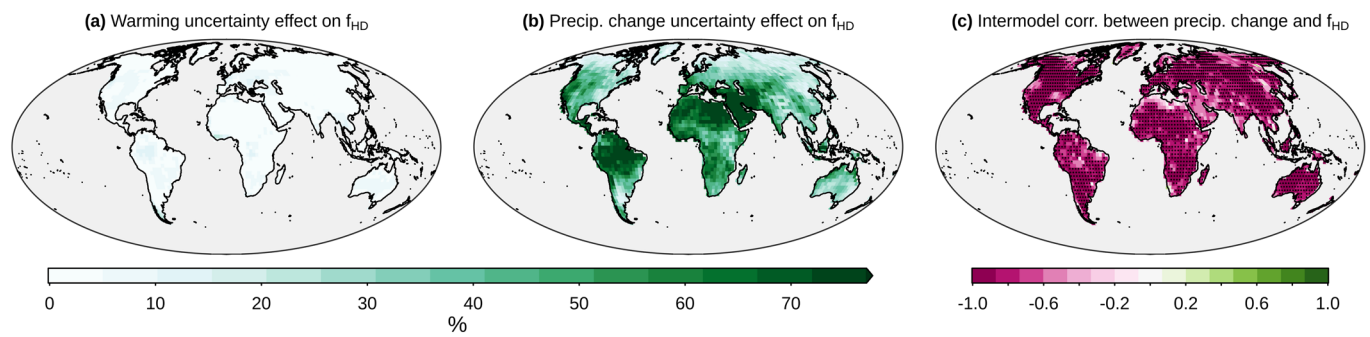
Extended Data Fig. 3 | Uncertainty in the frequency of compound hot-dry events (f_{HD}) in idealised experiments. (Note that an in-depth interpretation of the figure is provided in the Supplementary Material.) Given a present-day bivariate Gaussian distribution of temperature T and precipitation P with a correlation $\text{cor}(T, P)$ of -0.5 (first row), 0 (second row), and 0.5 (third row), shading shows the uncertainty in the future f_{HD} associated with uncertainty in the change of mean temperature (left column) and mean precipitation (right column) at given levels of expected changes in mean temperature (shown on the x-axis) and mean precipitation (y-axis). Magenta isolines show the expected f_{HD} resulting from the expected changes in mean temperature and precipitation (they are the same on right and left columns for a given $\text{cor}(T, P)$). The second axes show changes in units of present-day standard deviations. The closed contour shows the kernel density containing 90% of the multimodel mean projected changes in mean temperature and precipitation in units of relative present-day standard deviations over land grid-points (actual changes in °C and mm/day are shown in Extended Data Figure 2b and 7b, respectively). The green line indicates changes of equal magnitude in temperature and precipitation, in units of present-day standard deviations. (Note that the difference in magnitude of uncertainty from temperature (left column) and precipitation (right column) results from the fact that the uncertainty in the change of temperature is relatively large compared to the uncertainty in the change of precipitation).



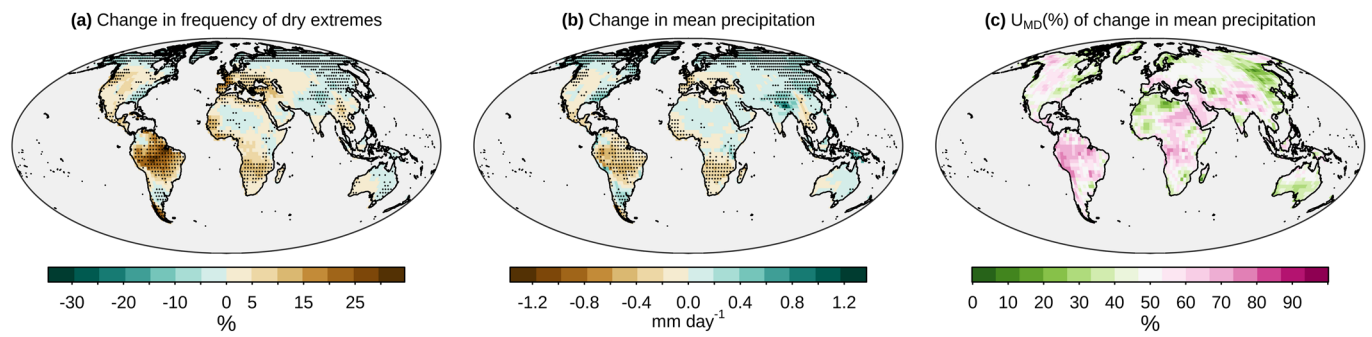
Extended Data Fig. 4 | Effect of uncertainty in local warming and precipitation or soil moisture trends on future f_{HD} . **a-b**, The same as Fig. 3c,f, but for extreme events of temperature and precipitation that are defined as values above and below their individual 95th and 5th percentiles, respectively. **c-d**, The same as Fig. 3c,f, but when considering compound hot-dry events during the wettest, instead than the hottest, season. **e-f**, The same as Fig. 3c,f, but when considering soil moisture rather than precipitation and based on four rather than seven available climate models.



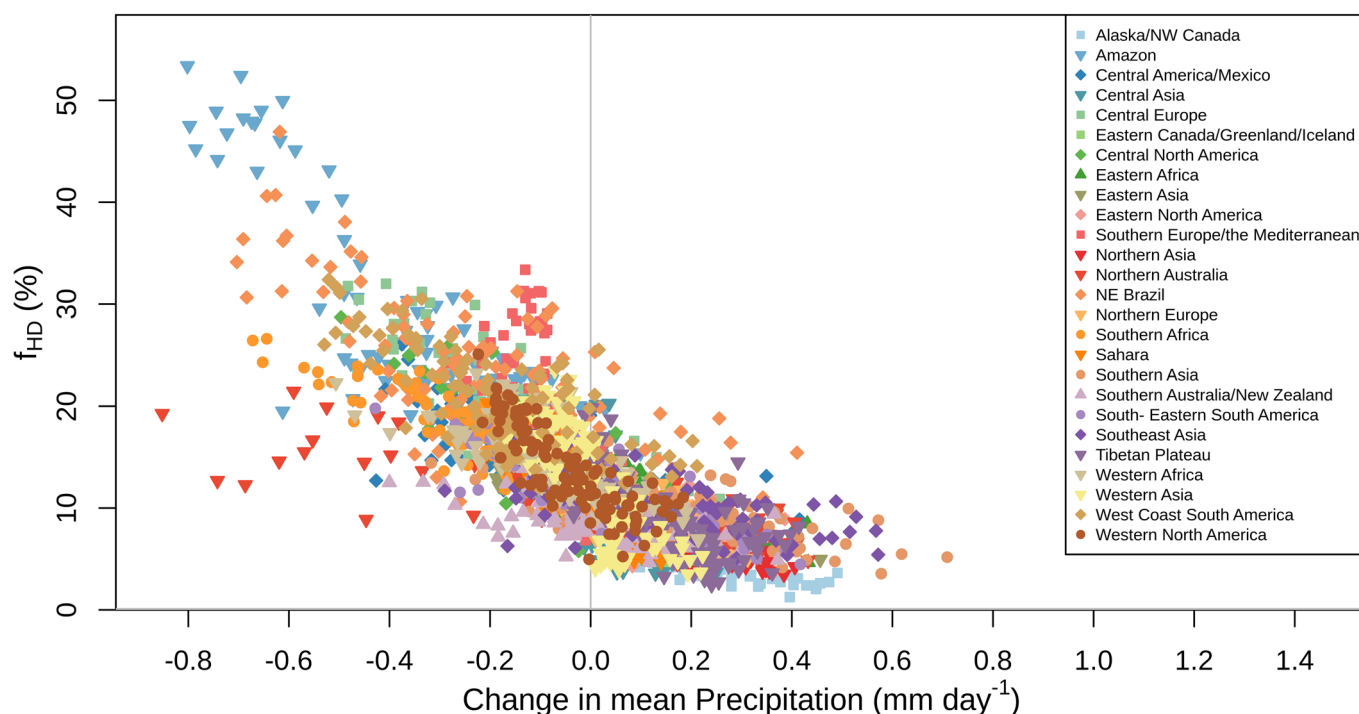
Extended Data Fig. 5 | Correlation between the future frequency of compound hot-dry events (f_{HD}) and changes in mean temperature and precipitation in idealised experiments. (Note that an in-depth interpretation of the figure is provided in the Supplementary Material.) Pairs of temperature T and precipitation P are simulated from a bivariate Gaussian distribution with a given $\text{cor}(T, P)$ which considers an expected future change in mean precipitation and temperature and variability around this change. For a given mean temperature change of $+2^\circ\text{C}$ and no change in mean precipitation, panel **a,b** show how future f_{HD} depends on the exact change in temperature and precipitation, respectively (given $\text{cor}(T, P) = -0.5$). For different values of $\text{cor}(T, P)$ of -0.5 (**c,d**), 0 (**e,f**), and 0.5 (**g,h**), shading shows the correlation between the future f_{HD} and the change in temperature (left column) and precipitation (right column) at given levels of expected changes in mean temperature (shown on the x-axis) and mean precipitation (y-axis). For example, the correlation coefficient of the pairs in **a** is reported in panel **c**. Axes, green lines, and closed contours are the same as in Extended Data Figure 3. Stippling indicates where at least 90% of the f_{HD} values from the Gaussian distribution are equal to 0%.



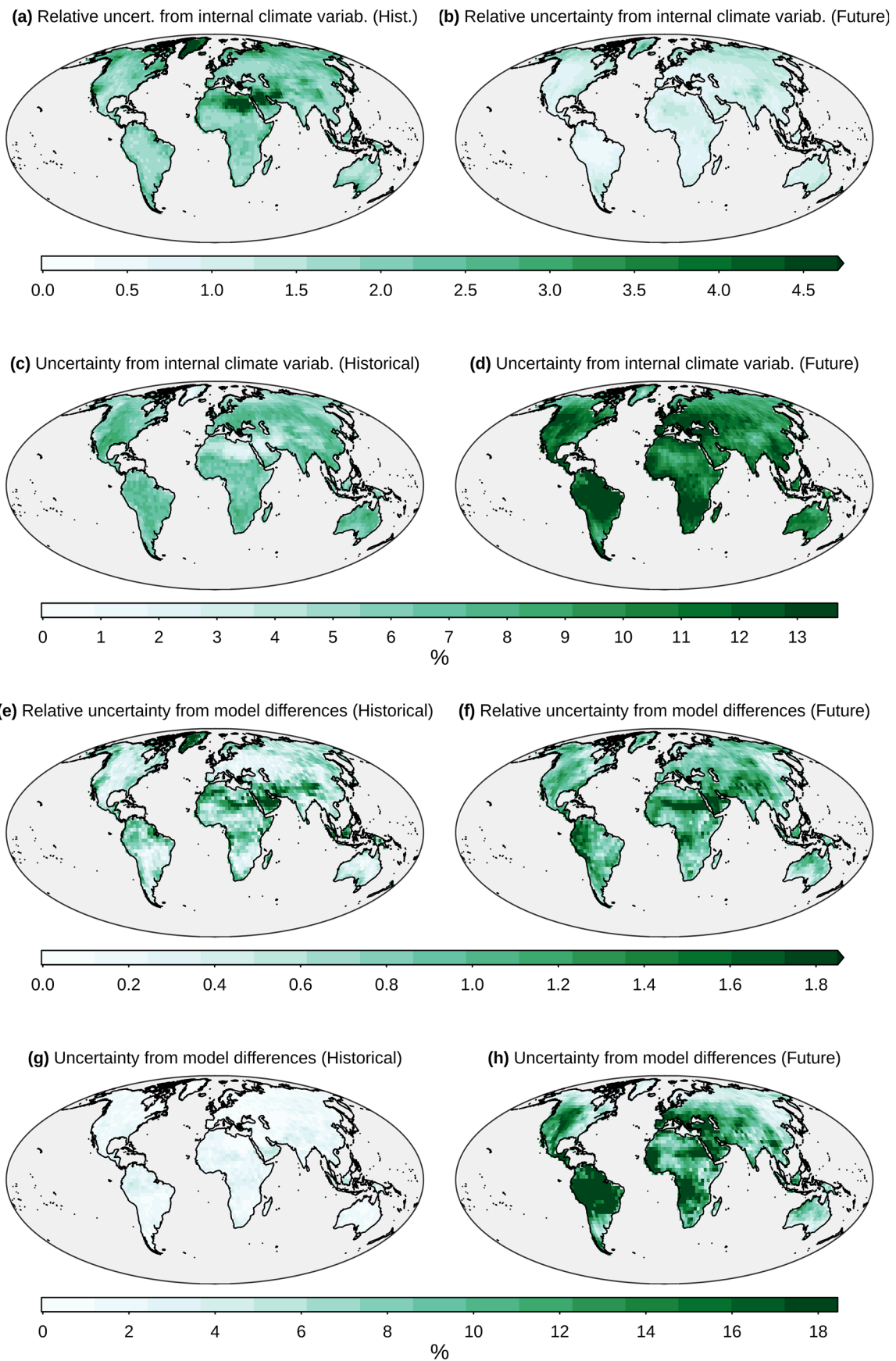
Extended Data Fig. 6 | Effect of uncertainty in local warming and precipitation trends on future f_{HD} under no dependence between temperature and precipitation. The same as Fig. 3c,e,f, but in a scenario within which the warm-season mean temperature T and precipitation P time series are uncorrelated. That is, for each model ensemble member, the thirty-one pairs (T,P) of the period 1950–1980 and in the warmer climate period are randomly shuffled prior to proceeding with the rest of the analysis.



Extended Data Fig. 7 | Precipitation changes in a world 2 °C warmer than pre-industrial conditions and associated drivers of uncertainties. The same as Extended Data Figure 2, but for precipitation.

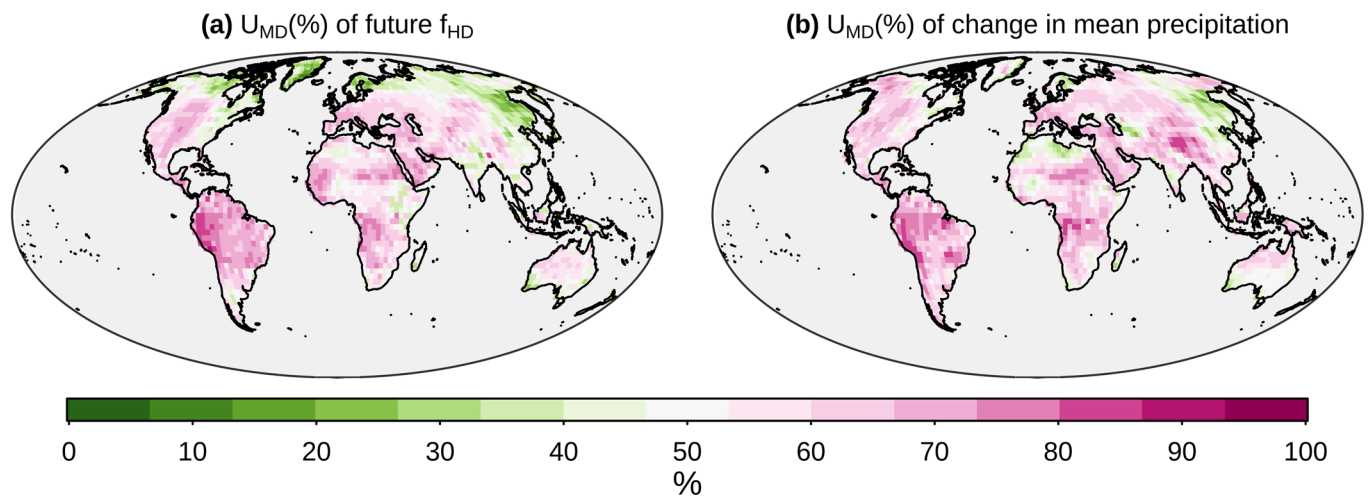


Extended Data Fig. 8 | Relationship between regional future frequency of compound hot-dry events (f_{HD}) and mean precipitation trends. Similar to Fig. 4, but for all of the regions used in the Intergovernmental Panel on Climate Change (IPCC). That is, in a world 2 °C warmer than pre-industrial conditions, regionally averaged future f_{HD} against changes in mean precipitation (relative to 1950-1980) are shown for all IPCC regions (differentiated by colored symbols), based on a pool of ensemble members from different climate models (Methods). The image highlights that the relationship is non-linear, in line with theoretical expectations (Figure Extended Data Figure 5b). Such a non-linear behaviour is not well evident when considering individual regions given the more limited range of uncertainty of precipitation trends.



Extended Data Fig. 9 | See next page for caption.

Extended Data Fig. 9 | Sources of uncertainty in the frequency of compound hot-dry events (f_{HD}) in the historical period and in the future (a world 2 °C warmer than pre-industrial conditions). **a,b**, Uncertainty due to internal climate variability ($2 \times U_{\text{IV}}$) relative to f_{HD} in the historical and future periods, respectively. Panel **a** is the same as Fig. 1c. **c,d**, Uncertainty due to internal climate variability ($2 \times U_{\text{IV}}$) in historical and future periods, respectively. **e,f**, Uncertainty in f_{HD} due to model-to-model differences ($2 \times U_{\text{MD}}$) relative to f_{HD} in the historical and future periods, respectively. **g,h**, Uncertainty in f_{HD} due to model-to-model differences ($2 \times U_{\text{MD}}$) in the historical and future periods, respectively.



Extended Data Fig. 10 | Drivers of uncertainties in future frequency of compound hot-dry events (f_{HD}) and mean precipitation trends in a world 3 °C warmer than pre-industrial conditions. a,b, As in Fig. 2b and Extended Data Figure 7c, respectively, but in a world 3 °C warmer than pre-industrial conditions. That is, uncertainty due to model-to-model differences (U_{MD}) relative to the sum of U_{IV} (uncertainty due to internal climate variability) and U_{MD} for future f_{HD} in **a** and mean precipitation trends in **b**. U_{MD} is larger than U_{IV} over 67% and 77% of landmasses for future f_{HD} and mean precipitation trends, respectively.